

See discussions, stats, and author profiles for this publication at: <https://www.researchgate.net/publication/259313743>

Structural Parameters Controlling the Fluorescence Properties of Phytochromes

ARTICLE in BIOCHEMISTRY · DECEMBER 2013

Impact Factor: 3.02 · DOI: 10.1021/bi401287u · Source: PubMed

CITATIONS

4

READS

73

10 AUTHORS, INCLUDING:



Tillmann Utesch

Technische Universität Berlin

24 PUBLICATIONS 237 CITATIONS

SEE PROFILE



Franz-Josef Schmitt

Technische Universität Berlin

55 PUBLICATIONS 439 CITATIONS

SEE PROFILE



Andrea Mroginski

Technische Universität Berlin

73 PUBLICATIONS 1,095 CITATIONS

SEE PROFILE



Thomas Friedrich

Technische Universität Berlin

89 PUBLICATIONS 2,808 CITATIONS

SEE PROFILE

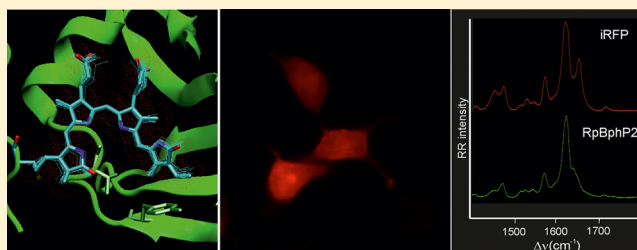
Structural Parameters Controlling the Fluorescence Properties of Phytochromes

Francisco Velazquez Escobar,[§] Thomas Hildebrandt,[§] Tillmann Utesch, Franz Josef Schmitt, Ina Seuffert, Norbert Michael, Claudia Schulz, Maria Andrea Mroginski, Thomas Friedrich, and Peter Hildebrandt*

Technische Universität Berlin, Institut für Chemie, Sekr. PC14, Straße des 17. Juni 135, D-10623 Berlin, Germany

S Supporting Information

ABSTRACT: Phytochromes constitute a class of photoreceptors that can be photoconverted between two stable states. The tetrapyrrole chromophore absorbs in the red spectral region and displays fluorescence maxima above 700 nm, albeit with low quantum yields. Because this wavelength region is particularly advantageous for fluorescence-based deep tissue imaging, there is a strong interest to engineer phytochrome variants with increased fluorescence yields. Such targeted design efforts would substantially benefit from a deeper understanding of those structural parameters that control the photophysical properties of the protein-bound chromophore. Here we have employed resonance Raman (RR) spectroscopy and molecular dynamics simulations for elucidating the chromophore structural changes in a fluorescence-optimized mutant (iRFP) derived from the PAS-GAF domain of the bacteriophytochrome RpBphP2 from *Rhodospseudomonas palustris*. Both methods consistently reveal the structural consequences of the amino acid substitutions in the vicinity of the biliverdin chromophore that may account for lowering the probability of nonradiative excited state decays. First, compared to the wild-type protein, the tilt angle of the terminal ring D with respect to ring C is increased in iRFP, accompanied by the loss of hydrogen bond interactions of the ring D carbonyl function and the reduction of the number of water molecules in that part of the chromophore pocket. Second, the overall flexibility of the chromophore is significantly reduced, particularly in the region of rings D and A, thereby reducing the conformational heterogeneity of the methine bridge between rings A and B and the ring A carbonyl group, as concluded from the RR spectra of the wild-type proteins.



The technological developments in fluorescence microscopy in the past years have prompted substantial efforts for exploiting these methods in biology.^{1–3} Using chemically attached fluorescent dyes, it is possible to monitor specific target biomolecules with a high sensitivity down to the single-molecule level and a spatial resolution beyond the diffraction limit. The chemical modification of biomolecules is, however, only of limited applicability for probing cellular processes. As an alternative for in vivo studies, genetically encoded fluorescent proteins or cofactor-protein complexes are used as optical markers by generating fusion constructs with the proteins of interest.^{1,4–7} Widely used genetically encoded fluorescence markers are the green-fluorescent protein (GFP), originally isolated from the marine jellyfish *Aequorea victoria* and its engineered spectral variants, as well as its homologues from other species, which today cover nearly the whole visible spectrum.^{1–3} A substantial drawback of these GFP-derived fluorescent labels is the restriction of the “working” range to the visible spectral region, where they compete with the absorption and emission properties of various natural pigments. Moreover, the significant overlap between their excitation and emission spectra limits the possibilities for spectral demultiplexing in order to discriminate the spatial distribution or the interaction patterns of a larger number of fluorophore-tagged target

molecules. Although in the blue spectral range, problems arise from significant overlap with cellular autofluorescence, the red region suffers from the limited number of available fluorescent proteins, which additionally exhibit limited brightness or photostability.³ Thus, there is still a high demand for additional and improved red and far-red fluorophores to expand the toolkit of fluorescence microscopy and to take benefits from the superior signal-to-noise ratio in this spectral range. To fulfill these necessities, it is highly desirable to utilize photoreceptors absorbing and emitting in the near-infrared optical window.

Biliproteins such as phytochromes fulfill these spectral requirements because the tetrapyrrole cofactor absorbs between 660 and 700 nm and fluorescence maxima are above 700 nm.⁸ Phytochromes act as photoswitches between two (meta)stable states that are denoted as Pr and Pfr, according to the red and far-red absorption maxima of the chromophore. Photoinduced interconversion between these parent states is linked to the activation or deactivation of a catalytic module, frequently a histidine kinase.

Received: September 15, 2013

Revised: December 4, 2013

Published: December 16, 2013



However, natural phytochromes have an intrinsically low fluorescence quantum yield of usually less than 2%.⁹ As a consequence, significant efforts have been made to genetically engineer variants of bacterial phytochromes, carrying a covalently bound biliverdin (BV) cofactor, to improve the fluorescence properties by increasing the quantum yield, raising the extinction coefficient, and shifting the fluorescence maximum further to the near-infrared. First successful examples have been generated on the basis of the chromophore binding domain (CBD) of bacteriophytochromes.^{4–6} The IFP1.4 variant of DrBphP from *Deinococcus radiodurans* showed an increase of the fluorescence yield from 1.9 to about 7%,⁵ and similar or even higher yields of ca. 6% and 11% were obtained for constructs engineered from the *Rhodospseudomonas palustris* bacteriophytochrome RpBphP2 and RpBphP6, respectively.^{4,6} Although these values are still by far inferior to those of GFP variants, the spectral properties are likely to improve by further genetic optimization. In addition, these far-red chromophores enable novel means of noninvasive deep-tissue monitoring by rapidly emerging photoacoustic tomography or imaging techniques.^{5,10}

It is therefore of particular interest to analyze those structural parameters that control the fluorescence quantum yield and the energies of electronic absorption and fluorescence of BV in phytochromes. In this respect, the recent crystallographic analysis of fluorescing CBD variants of DrBphP constitutes an important basis for correlating photophysical properties of the cofactor with structural changes at the chromophore binding site induced by amino acid substitutions.⁹ Additional information on the excited-state reactions can be derived from ultrafast spectroscopy, as recently shown for mutants of RpBphP2 and RpBphP3.^{11–14}

In this work, we have employed resonance Raman (RR) spectroscopy, combined with molecular dynamics (MD) simulations, to analyze the ground state conformation of the cofactor and its intermolecular interactions within the chromophore binding pocket. Here, we have used these techniques to identify structural changes of the BV chromophore in the fluorescence-optimized mutant iRFP, which was recently used for deep-tissue imaging in mice.⁴ The mutant is derived from the two-domain PAS-GAF fragment of RpBphP2 (termed PG-P2 herein), lacking the PHY domain that is required for the proper phototransformation between the parent states Pr and Pfr and, thus, for its natural biological function.

MATERIALS AND METHODS

Cloning Strategy. For the expression of holophytochrome, we constructed three plasmids bearing the coding sequence for different apo-phytochromes and one plasmid with a heme oxygenase for in-cell biliverdin synthesis. The amino acid sequence of RpBphP2¹⁵ was adopted from Uniprot Q6N5G3 and the iRFP sequence from Filonov et al.¹⁰ cDNAs for RpBphP2 amino acids 1–501 (PAS-GAF-PHY, termed PGP-P2 herein) and iRFP (316 AS) were generated by commercial gene synthesis (GeneArt, Life Technologies) using the GeneOptimizer algorithm to optimize codon usage for expression in mammalian cells (sequences available on request).¹⁶ To obtain the PAS-GAF fragment of RpBphP2 (amino acids 1–316; termed PG-P2 herein), an appropriate stop codon was introduced into the RpBphP2 1–501 cDNA. The cDNAs were excised by *Bam*HI and *Not*I and ligated in frame into a modified pQE81L-Amp vector (Qiagen) carrying

an ampicillin resistance gene and harboring an engineered *Not*I restriction site. This resulted in protein sequences with an N-terminal 6xHis tag (N-terminal sequence MRGSHHHHHH-TDPAT) preceding the start methionine of the iRFP, PG-P2, and PGP-P2 sequences.

The cDNA of the human heme oxygenase type 2 (hHox2) was amplified from the IMAGE consortium clone IMAGE:2821444 by PCR, using primers harboring *Sph*I and *Kpn*I restriction sites. The PCR fragment was restricted with *Sph*I and *Kpn*I and ligated in frame into the similarly cut pQE81L-Kan vector, which carries a kanamycin resistance gene. The complete open reading frame of hHox2 cDNA sequence was verified by sequencing (Eurofins MWG Operon). To avoid copurification of hHox2 in Ni²⁺-sepharose column chromatography, the N-terminal 6xHis tag was deleted afterward, using the QuikChange mutagenesis kit (Stratagene). Deletion was verified by sequencing (Eurofins MWG Operon).

In order to accomplish biliverdin cofactor insertion into phytochromes already upon protein expression in *E. coli*, NEBturbo cells (New England Biolabs) were transformed with a 1:1 mixture of pQE81L-Kan plasmid with hHox2 and one of the pQE81L-Amp plasmids with iRFP, PG-P2, or PGP-P2 sequences. The transformed cells were grown overnight at 37 °C on LB-agar selection plates containing 50 µg/mL kanamycin and 50 µg/mL ampicillin.

Expression and Purification. For protein expression, 3 × 400 mL of LB-medium with kanamycin and ampicillin were inoculated from a preculture to 0.1 optical density (OD) and grown at 37 °C in an orbital shaker (200 rpm) to an OD of 0.6. After induction with 500 µM IPTG cells were grown for 24 h at 37 °C (iRFP and wild-type PG-P2) or at 20 °C for 48 h (wild-type PGP-P2). Cells were harvested by centrifugation, yielding deeply blue-green-colored pellets, indicating formation and integration of the intact BV cofactor into the bacteriophytochrome variants. Cell pellets were resuspended in phosphate buffer and lysed by two passages through a French press (18000 psi). After removal of the cell debris by centrifugation (24000g, 4 °C), the clarified supernatant was purified on Ni²⁺-Sephacolumns (GE-Healthcare) according to the manufacturer's manual (20 mM imidazole was supplemented to the supernatant as recommended). Purest fractions (SAR ≥ 1) were pooled and dialyzed against 50 mM Tris-HCl, 300 mM NaCl, 5 mM EDTA (pH 7.8).

For comparison, we have studied the bacteriophytochrome Agp1 from *Agrobacterium tumefaciens*. For this purpose, we have used a PAS-GAF-PHY variant in which the first nine N-terminal residues were deleted and three amino acids on the protein surface were substituted (F289A, M295A, and R296S). These modifications prevent dimerization but do not affect the optical properties or the photoinduced reaction cycle. This protein variant, denoted as Agp1, was expressed and purified as described previously.¹⁷

Buffer solutions used for the RR experiments included 50 mM Tris-HCl, 300 mM NaCl, 5 mM ethylenediaminetetraacetic acid in H₂O (D₂O) at pH (pD) of 7.8. Protein samples were concentrated via Microcon filters up to a value corresponding to an optical density of ca. 40 at 280 nm (ca. 10 mg/mL).

Spectroscopic Measurements. RR measurements were performed using a Bruker Fourier-transform Raman spectrometer RFS 100/S with 1064 nm excitation (Nd:YAG cw laser, line width 1 cm⁻¹) equipped with a nitrogen-cooled cryostat from Resultec (Linkam). The spectra were measured at –140

or +10 °C with a laser power at the sample of 780 mW. In order to identify potential laser-induced damage of the phytochrome samples, spectra before and after a series of measurements were compared. In no case were changes between these control spectra determined. For each spectrum, the accumulation time was 1 h. Protein and buffer Raman bands were subtracted on the basis of a Raman spectrum of apo-phytochrome (Supporting Information, Figure S1). The pure spectra were further analyzed by a band fitting procedure assuming Lorentzian band shapes. H/D exchange involved 5 washing steps with D₂O or H₂O buffer solution (30 min centrifugation at 10000g per step).

Stationary fluorescence spectra were measured with 670 nm excitation in a temperature range from +10 to −140 °C. Further details are given in the Supporting Information.

Molecular Dynamics Simulations. The classical atomistic MD simulations on two monomeric model structures of the PAS-GAF fragment of RpBphP2, namely, the wild-type (WT) protein PG-P2 (PG-P2 model) and the fluorescent mutant iRFP described above (iRFP model), were performed with the NAMD2.7 software.^{18,19} The CHARMM27 force field²⁰ was employed to describe the apoprotein, and the force field parameters for the BV chromophore were extracted from Kaminski et al.²¹ The starting geometry for the PG-P2 model was taken from the crystallographic structure (PDB entry: 4e04). Because this structure corresponds to a mutated form of PG-P2,²² the PG-P2 model was generated by back-mutation of the crystal structure to the original sequence. For this, the Asn105 insertion was deleted and the following amino acids substitutions were attained: P98R, D99K, G100D, E101A, R102G, A103F, F104 V, R127A, Y128E, S135R, V136T, R137N, R237 V, E296D and V297G. Furthermore, the expression tag comprising residues 320 to 327 present in the crystal structure was removed. The iRFP model was constructed by mutating the PG-P2 model at 13 different sites: S13L, A92T, V104I, V114I, E161K, Y193K, F198Y, D202T, I203V, Y258F, A283 V, K288T and N290Y. The two structural models were protonated according to pH 7.0 using the PSFGEN-VMD plugin.²³ On the basis of the visual inspection of the corresponding environments, all histidine residues were protonated at the ϵ -nitrogen except for His285, which was modeled with a proton at the δ -nitrogen. The net charges of the proteins yield −13 and −10 e for the PG-P2 and the iRFP model, respectively. In order to remove bad contacts that may be present in the initial structural models due to mutations and deletion of amino acids, 5000 steps of energy minimization were performed using the conjugated gradient algorithm on the modified regions of each model in vacuum keeping the rest of the protein fixed. Both structural models were then solvated in cuboid boxes of TIP3P water molecules²⁴ with approximate dimensions of. 78 × 87 × 112 Å³ (23829 and 23822 water molecules for WT and iRFP models, respectively). In addition, the net charges of the proteins were compensated for by inserting chloride and sodium ions randomly at 25 mM ionic strength. Ionization of the models was carried out using the AUTOIONIZE plugin of VMD.²³ The MD simulations were run under periodic boundary conditions with extended electrostatics using the Particle Mesh Ewald Summation²⁵ with a cutoff distance of 12 Å for the van der Waals interactions and short-ranged electrostatics. The SHAKE algorithm²⁶ was applied to constrain all bond lengths between heavy atoms and hydrogen atoms assuring, in this way, a simulation step of 2 fs. The energies of the solvated systems were initially minimized

with the conjugated gradient integrator using decreasing harmonic constraints on the protein backbone and on the BV cofactor (from 25 to 5 kcal/(mol Å²)). After 60 ps heating using Langevin dynamics with decreasing position restraints on the heavy atoms of the protein cofactor (from 5 to 2.5 kcal/(mol Å²)), the entire system was equilibrated for another 60 ps. During the equilibration run, the harmonic constraints on the protein were gradually released until all atoms were allowed to move freely. Finally the dynamics of the two model systems were simulated for 100 ns at 300 K in an NPT ensemble under constant atmospheric pressure and temperature using the Langevin Piston method.²⁷ Convergence of the trajectories was checked in terms of energetics and root mean square deviations (rmsd) of the protein and the chromophore from the initial structural models. The statistical analysis of the structural properties during the last 40 ns of the MD trajectories was performed with the VMD software.²³

RESULTS

The iRFP mutant was generated from the D202H variant of the PAS-GAF domain of P2 by random mutagenesis, leading to 13 substitutions compared to the wild-type protein PG-P2. Among them, five substitutions (Y193K, F198Y, D202T, I203V, and Y258F) are located in the chromophore binding pocket (Figure 1). These substitutions are likely to be of primary importance

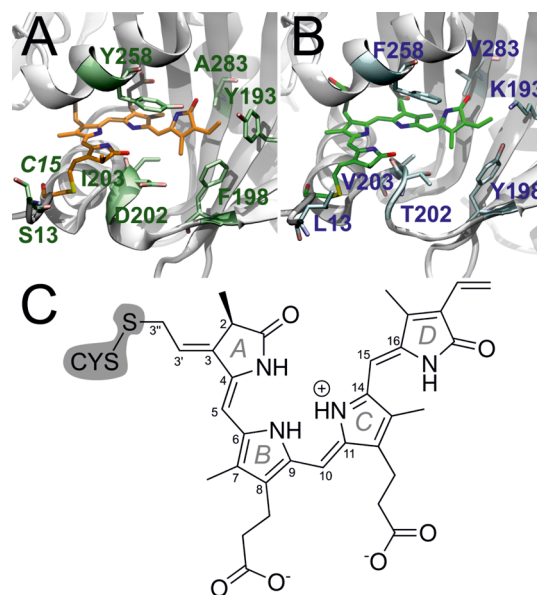


Figure 1. The chromophore binding pocket of (A) wild-type PG-P2 and (B) iRFP, as obtained by 100-ns MD simulations (see text for further details), and (C) the structural formula of the BV chromophore.

for the photophysical properties. For example, the replacement of the highly conserved D202 has been shown to impair photoisomerisation of the chromophore.²⁸ In fact, iRFP was found to be locked in the Pr state (data not shown). Thus, the comparison with the spectra of the wild-type proteins of RpBphP2 and Agp1 discussed in the following only refers to the Pr state.

Resonance Raman Spectroscopy. The overall vibrational band pattern of iRFP does not differ significantly from those of the Pr state of PG-P2 and PGP-P2 proteins and other prototypical BV-binding phytochromes (Figure S3, Supporting

Information). Thus, there are no indications for deviations from the overall *ZZZssa* chromophore geometry as determined for the Pr state of various phytochromes.^{29–31} Also, as in the Pr state of all prototypical phytochromes, the cofactor is in the cationic form with all four pyrrole nitrogens carrying a proton. A closer inspection of the spectra, however, reveals spectral differences in three regions as will now be discussed in more detail.

Figure 2 shows the spectral region from 1500 to 1700 cm^{-1} , which is dominated by modes involving the C=C stretching

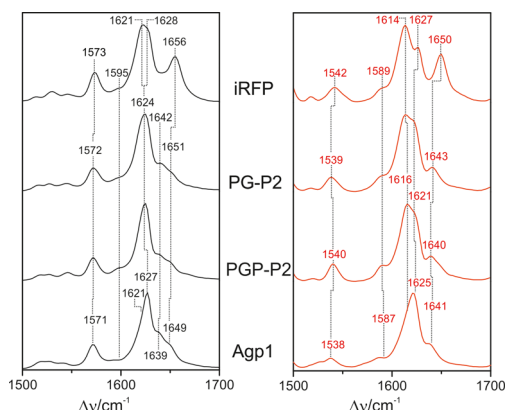


Figure 2. RR spectra of the Pr state of iRFP, PG-P2, PGP-P2, and Agp1 in the C=C stretching region, measured with 1064-nm excitation at -140°C . Spectra obtained from samples in H_2O (pH 7.8) and D_2O (pD 7.8) are shown on the left (black) and right panel (red), respectively.

coordinates of the methine bridges, ring *D*, and its vinyl substituent (see Figure 1 for ring numbering). Furthermore, the N—H in-plane bending (N—H ip) mode of the rings *B* and *C* gives rise to the band at 1573 cm^{-1} (iRFP), which is a characteristic marker for the protonated state of the cofactor. This band disappears upon H/D exchange and the corresponding counterpart, the N—D ip mode, is observed at 1079 cm^{-1} (Supporting Information, Figure S3).

We refer to previous vibrational analyses of the cofactor in phytochromes, carried out with experimental and theoretical methods, to disentangle the spectrally crowded region between 1590 and 1660 cm^{-1} .^{32–36} Accordingly, the most intense band is due to a mode dominated by the C=C stretching coordinate of the C—D methine bridge. As minor contributions of the N—H ip coordinate are involved, this mode undergoes a small downshift (5–8 cm^{-1}) upon H/D exchange. Thus, this mode is assigned to the 1621 cm^{-1} band in iRFP (1614 cm^{-1} in D_2O). The adjacent, nearly equally intense but H/D insensitive band is then ascribed to a C=C stretching mode of ring *D* although calculations predict only a low intensity.³⁵ Presumably, also the C—D stretching coordinate that is responsible for high RR activity contributes substantially to the mode at 1628 cm^{-1} . Frequency and intensity of the band at 1656 cm^{-1} and its 6 cm^{-1} downshift in D_2O are consistent with the assignment to the A—B stretching mode. The corresponding B—C stretching mode, which is only weakly Raman-active, is expected at much lower frequencies and, thus, is assigned to the weak shoulder at 1595 cm^{-1} .

Compared to iRFP, the spectra of the “non-fluorescing” phytochrome variants display two distinct differences. First, the ring *D* C=C stretching (at 1628 cm^{-1} of iRFP) appears at lower frequencies in PG-P2 and PGP-P2, whereas the C—D

stretching remains largely unchanged, as it can be clearly seen in the spectra measured from the proteins in D_2O (Figure 2, Supporting Information, Figure S5). In Agp1, the intensity ratio of the two bands is reversed, implying that the contribution of the C—D stretching coordinate to the higher frequency mode is even larger than in the case of the P2 protein variants. Second, the A—B stretching mode (at 1656 cm^{-1} in iRFP) is observed with a significantly reduced intensity and at a frequency lower by 5–7 cm^{-1} in PG-P2, PGP-P2, and Agp1. For these proteins, an additional nearby band at ca. 1640 cm^{-1} becomes detectable, which might originate from the C=C stretching of the ring *D* vinyl substituent. However, this mode is predicted to be essentially Raman-inactive such that, as an alternative assignment, both bands may be ascribed to A—B stretching modes originating from two conformers of the tetrapyrrole as previously suggested for Agp1.³⁷ A band fitting analysis suggests that this 1640 cm^{-1} band is also present in iRFP albeit with a much lower relative intensity with respect to the 1650 cm^{-1} band than in PG-P2, PGP-P2, and Agp1 (Supporting Information, Figure S4).

In the region between 600 and 900 cm^{-1} the most remarkable changes refer to the prominent 814 cm^{-1} band of iRFP (Figure 3). The frequency is higher by 4, 8, and 11 cm^{-1}

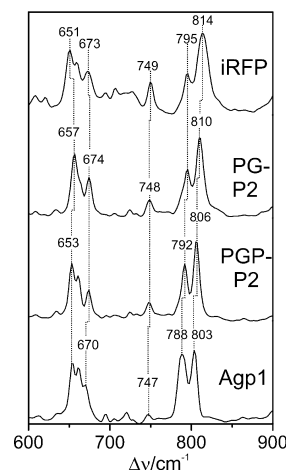


Figure 3. RR spectra of the Pr state of iRFP, PG-P2, PGP-P2, and Agp1 in the HOOP region, measured with 1064 nm excitation at -140°C . Spectra were obtained from samples in H_2O (pH 7.8).

compared to the PG-P2, PGP-P2, and Agp1 proteins, respectively. This band was assigned to the hydrogen-out-of-plane (HOOP) mode of ring *D* as confirmed by isotopic labeling and theoretical calculations.^{33,35} As a characteristic feature of phytochromes, this band is usually observed with relatively high RR intensity and its frequency has been shown to be correlated with the torsional angle of the C—D methine bridge.³⁵

Temperature-Dependent Spectral Changes. The RR spectra of iRFP and PG-P2 show only a weak temperature dependence. Upon increasing the temperature from -140°C to $+10^\circ\text{C}$, many bands display a slight broadening, in some cases accompanied by small frequency shifts that usually, however, do not exceed 3 cm^{-1} (Supporting Information, Figures S6–S8). Specifically, there is no indication for a redistribution of band intensities for those bands in the methine bridge stretching region that have been suggested to represent conformational substates. This is also true for the HOOP mode

at ca. 800 cm^{-1} that in the Pfr state of prototypical phytochromes was found to be the most sensitive marker for a temperature-dependent conformational equilibrium.³⁵ Most remarkably, the 814 cm^{-1} band of iRFP, which already displays a large bandwidth at low temperature (18 cm^{-1}), is not further broadened at room temperature and also the symmetric band shape remains unchanged. This is quite in contrast to the substantial broadening of the 810 cm^{-1} band of PG-P2 from 10 cm^{-1} (−140 °C) to 14 cm^{-1} (+10 °C) ((Figure 4).

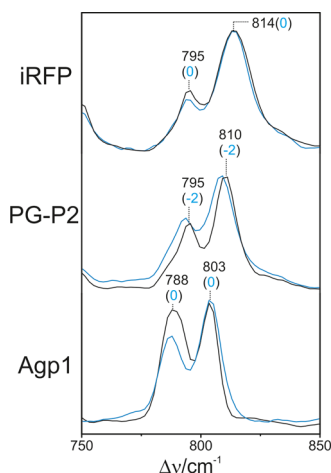


Figure 4. RR spectra of iRFP, PG-P2, and the Pr state of Agp1 measured with 1064 nm excitation. The black and blue traces refer to the measurements at −140 °C and +10 °C, respectively. Black labels refer to the peak positions at −140 °C. The blue numbers in parentheses indicate the shift of the peaks at +10 °C. Intensities are normalized to the strongest band in each spectrum.

In the region of the torsional and deformation modes between 650 and 680 cm^{-1} , all proteins show a similar behavior (Supporting Information, Figure S8). Here, the slight frequency shifts and band broadening are accompanied by distinct changes of the relative intensities in the room temperature spectra, reflecting a higher mobility of the chromophores in the binding pocket at room temperature.

Also the temperature-dependence of the fluorescence is very similar for iRFP and PG-P2. Upon decreasing the temperature from +10 to −140 °C, the fluorescence intensity, measured with 670 nm excitation, increases by up to an order of magnitude in both cases (Supporting Information, Figure S10). Taking into account that this factor refers to the uncorrected intensities (i.e., refractive index change and higher amplitude of the scattered light due to the formation of ice microcrystals during freezing), the intrinsic temperature-dependent increase of the fluorescence yield is lower.

The RR spectrum of Agp1 displays more pronounced temperature-dependent changes in the HOOP region (Supporting Information, Figure S8) because—unlike with iRFP and PG-P2—the intensity ratio of the two bands at 788 and 803 cm^{-1} varies quite substantially with the temperature (Figure 4). It might be that these two bands correspond to C—D methine bridge HOOP modes of two conformers such that the intensity changes reflect a temperature-dependent conformational equilibrium in analogy to the Pfr state of Agp1.³⁵

Carbonyl Stretching Modes. An important marker for protein-tetrapyrrole interactions are the two C=O stretching modes of ring A and D in the region between 1680 and 1740 cm^{-1} . Because in prototypical BV-binding phytochromes, the

carbonyl function of ring A is, unlike ring D, not linked to the conjugated π -electron system of the tetrapyrrole (Figure 1), the ring A C=O stretching mode appears at higher frequencies.³⁸ For the same reason, the RR intensity of this mode is much lower than that of the ring D C=O stretching such that only this latter mode can readily be identified in the low-temperature RR spectra of all proteins in H₂O (Figure 5). This mode is

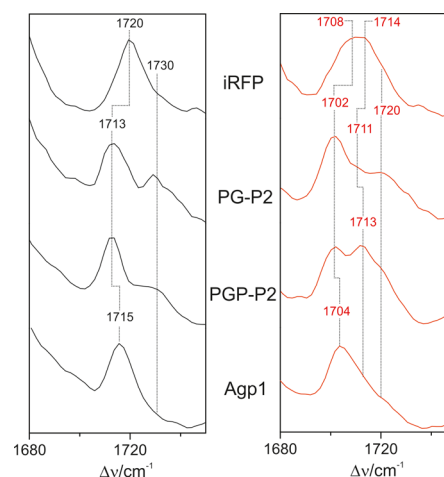


Figure 5. RR spectra of the Pr state of iRFP, PG-P2, PGP-P2, and Agp1 in the C=O stretching region measured with 1064 nm excitation at −140 °C. Spectra obtained from samples in H₂O (pH 7.8) and D₂O (pD 7.8) are shown on the left (black) and right panel (red), respectively.

observed at very similar positions (1713–1716 cm^{-1}) for all “non-fluorescing” protein variants but at a distinctly higher frequency (1720 cm^{-1}) for iRFP. In the case of PG-P2 (PGP-P2), the weak shoulder at ca. 1730 cm^{-1} is attributed to the ring A C=O stretching, whereas this mode can hardly be detected in Agp1 and iRFP. Upon raising the temperature to +10 °C, the bands of the ring D C=O stretching mode broaden for all proteins, accompanied by small frequency downshifts as observed for other tetrapyrrole modes (vide supra). As a consequence, the weak C=O stretching of ring A becomes also visible in the spectrum of iRFP at ca. 1730 cm^{-1} (Supporting Information, Figure S9). This mode remains essentially Raman-inactive in Agp1, but it can be detected at the same position in the IR “Pr–minus–Pfr” difference spectrum. Note that the IR difference spectra for PG-P2 and PGP-P2 (not shown) also support the assignments of the C=O stretching, in agreement with the previously published data by Toh et al.¹²

The frequencies of the C=O stretching modes depend on the (hydrogen bond) interactions of the carbonyl function with its immediate environment and on the coupling of the C=O stretching and N—H ip coordinates. This coupling, which may vary with structural perturbations of the respective pyrrole ring, is also the origin for the distinct H/D sensitivity of these modes. In fact, in D₂O, both modes shift down to lower frequencies but, most remarkably, the altered normal mode composition leads, in general, to a relative intensity increase of the ring A C=O stretching mode (Figure 5). Thus, it is even possible to identify two band components of this mode at ca. 1711–1714 cm^{-1} and ca. 1720 cm^{-1} , albeit with different relative intensities for the four proteins. In PG-P2, both components display comparable intensities whereas in iRFP the higher frequency component is much weaker. The downshift of

the ring *D* C=O stretching is essentially the same (11–12 cm^{-1}) in all four proteins.

Molecular Dynamics Simulations. The stability of the structural models for the wild-type PG-P2 protein and the iRFP mutant was initially checked by analyzing the evolution in time of the root mean square deviation (rmsd) of all carbon α atoms of the protein and of all heavy atoms belonging to the biliverdin chromophore (Figure 6). A plateau is reached within the first

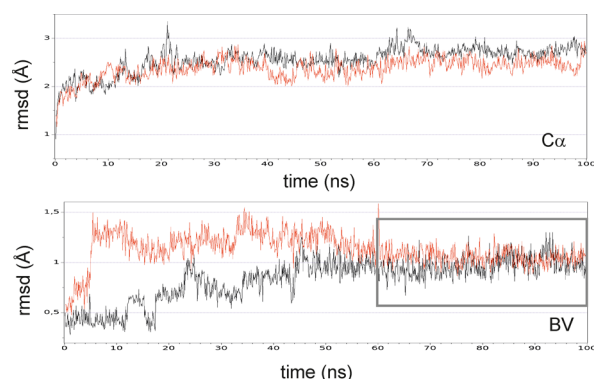


Figure 6. Evolution of the root mean square deviation (rmsd) for the $C\alpha$ atoms (top) and the heavy atoms of the BV chromophore (bottom) of PG-P2 during the 100 ns MD simulation. Black and red traces refer to the PG-P2 and iRFP model, respectively.

20 ns, with a mean rmsd value of 2.7 Å and 2.4 Å for the PG-P2- and the iRFP-models, respectively. The rmsd of the chromophore atoms, however, converge only after 60 ns MD simulation reaching a mean value of 1.0 Å for both models. For this reason, the statistical analysis of the MD trajectories was restricted to the last 40 ns because in this time span, we can assume that the protein and the chromophore reached a thermodynamic equilibrium.

The structural differences between PG-P2 wild-type protein and the iRFP mutant and their dynamic properties were analyzed by following the time evolution of selected structural parameters, such as the tilt angles between pyrrole rings and the bond and torsional angles of the BV methine bridges, and by computing their statistical distribution. In addition, the root mean square fluctuations (rmsf) of selected atoms of the BV chromophore were calculated in order to estimate and quantify the mobility of the chromophore atoms in the binding pockets of the two structural models.

The frequency distribution (counts) of the three tilt angles between adjacent pyrrole rings is shown in the Supporting Information (Figure S11), and the mean values and corresponding standard deviations are listed in Table 1. In the case of the rings *B* and *C*, there is no difference between the tilt angles computed for the PG-P2 and iRFP models, indicating that mutations of the chromophore binding pocket do not significantly alter the orientation of the two inner rings with respect to each other. This is, however, not the case for rings *A* and *B* and rings *C* and *D*. Although the *A*–*B* tilt angle decreases from 24° in the PG-P2 model to 21° in the iRFP model, the *C*–*D* tilt angle increases by ca. 8°. For both tilt angles, the standard deviations predicted for the PG-P2 structure are slightly higher (1°) than those computed for the mutant, reflecting a slightly restricted flexibility of the outer rings of the tetrapyrrole chromophore in the iRFP model (vide infra). The analysis of the torsional angles at the methine bridges (Supporting Information, Figure S12) shows that the

Table 1. Selected Structural Parameters of the BV Chromophore in the PG-P2 and iRFP Models.^a

	WT	iRFP
Bond Lengths		
C(4)=C(5)	1.3654 (0.03)	1.3647 (0.03)
C(5)—C(6)	1.4262 (0.03)	1.4229 (0.03)
C(9)—C(10)	1.3802 (0.03)	1.3782 (0.03)
C(10)—C(11)	1.3767 (0.03)	1.3780 (0.03)
C(14)—C(15)	1.4254 (0.03)	1.4267 (0.03)
C(15)=C(16)	1.3651 (0.03)	1.3681 (0.03)
Bond Angles		
C(4)—C(5)—C(6)	20.5 (7.7)	16.6 (6.3)
C(9)—C(10)—C(11)	−5.1 (5.8)	−6.8 (6.5)
C(14)—C(15)—C(16)	−106.8 (13.5)	−111.8 (9.6)
Dihedral Angles		
N(A)—C(4)=C(5)—C(6)	15.8 (6.9)	15.0 (7.4)
C(4)=C(5)—C(6)—N(B)	9.2 (8.3)	5.5 (7.8)
N(B)—C(9)—C(10)—C(11)	7.1 (8.5)	−3.0 (8.6)
C(9)—C(10)—C(11)—N(C)	−13.3 (8.6)	−5.5 (9.5)
N(C)—C(14)—C(15)=C(16)	−125.5 (10.3)	−137.1 (8.3)
C(14)—C(15)=C(16)—N(D)	14.5 (9.4)	17.0 (9.3)
Tilt Angles		
A—B	24.0 (7.5)	21.0 (6.5)
B—C	11.3 (5.0)	10.7 (4.9)
C—D	116.8 (8.2)	124.2 (7.1)

^aMean values and corresponding standard deviations (in brackets) were computed for the last 40 ns of the MD trajectory. Bond lengths are given in Å and angles in degrees. Coordinates are defined according to inset of Figure 6.

changes of the tilt angles between the pyrrole rings are mainly due to twists of the C—C single bond at the corresponding methine bridge. Although there is no variation of the *B*–*C* tilt angle upon mutation, the torsional angles at the *B*–*C* methine bridge differ significantly between the two protein models. In particular, the mean values for the N(*B*)—C(9)—C(10)—C(11) and C(9)—C(10)—C(11)—N(*C*) torsional angles of the PG-P2 model, which are higher than those predicted for iRFP, point to a stronger distortion of the *B*–*C* methine bridge in the wild-type protein. Other important structural parameters, which may strongly influence the spectroscopic pattern in the fingerprint region, are the bond angles and the C—C bond lengths at the tetrapyrrole methine bridges. The statistical distribution of the bond angles during the last 40 ns are plotted in Figure S13 (Supporting Information). In average, there is a decrease of the C(4)—C(5)—C(6) bond angle in the iRFP mutant compared to the wild-type protein together with a slight shortening of the C(4)=C(5) bond and the elongation of the C(5)—C(6) bonds, reflecting a weakening of the π -electron conjugation at the *A*–*B* methine bridge. Such changes in the electron density of the *A*–*B* bridge should shift the vibrational frequency of the C=C stretching mode to higher values, as it is in fact observed in the experimental RR spectra (Figure 2). In a similar way, the slightly elongated C=C bond at the *C*–*D* methine bridge of iRFP may explain the 3 cm^{-1} downshift of the *C*–*D* stretching frequency compared to the wild-type protein.

The rmsf values computed for the backbone atoms of the BV chromophore of the PG-P2 and iRFP models over the last 40 ns of the MD simulation are larger for the PG-P2 model compared to those of the iRFP mutant, especially in the regions

corresponding to ring A (atoms 1–4) and ring D (atoms 16–21) (Figure 7).

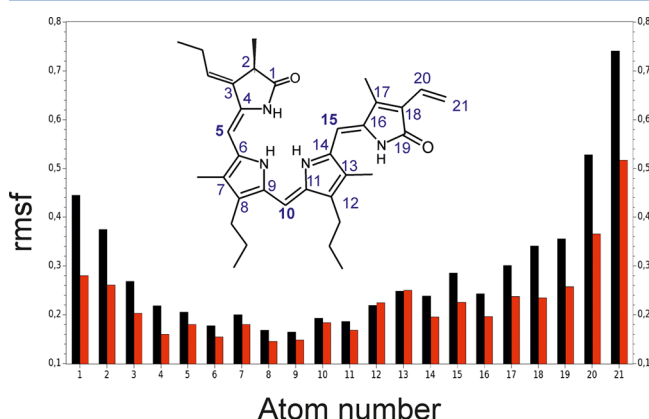


Figure 7. Root mean square fluctuations (rmsf) of heavy atoms in the BV chromophore. Inset: Structural formula of BV indicating the heavy atoms considered for the rmsf plot in blue.

DISCUSSION

Structural Changes in the iRFP Variant Protein. The analysis of the RR spectra together with the results of the MD simulations indicate that the structural changes brought about by the amino acid substitutions in iRFP primarily refer to the C—D and A—B methine bridges as well as to the respective terminal rings A and D including their carbonyl functions.

The most sensitive spectral marker for structural changes at the C—D methine bridge is the HOOP mode at ca. 800 cm^{-1} . Its frequency is inversely correlated with the C(14)—C(15)—C(16)—N(D) dihedral angle as previously determined for the Pfr state of the BV-binding PaBphP.³⁵ The significant frequency upshift of this mode in iRFP (800 cm^{-1}) compared to the other protein variants indicates an increase of this angle, consistent with the MD simulations that predict a slightly increased tilt angle of ring D with respect to ring C. This structural perturbation is attributed to two factors. First, the Y193K and F198Y substitutions cause structural changes in chromophore binding pocket that primarily involve the immediate environment of ring D, thereby affecting the C—D methine bridge geometry (Supporting Information, Figure S14). In this way, the side chain of Tyr198 comes in close contact to ring D which also provides an explanation for the unusually broad and temperature-independent bandwidth of the C—D methine bridge HOOP mode. The spatial proximity of the aromatic ring of Tyr198 to the C—D methine bridge and the small energy difference between the HOOP mode at 814 cm^{-1} of the chromophore and the tyrosine ring breathing mode³⁹ at ca. 830 cm^{-1} may allow for vibrational energy transfer from the chromophore to Tyr198 which is reflected by the broadening of the HOOP mode. A similar mechanism was shown to account for the band broadening of the C=N stretching mode of the retinal chromophore in bacteriorhodopsin.⁴⁰ Second, the substitution of Tyr258 by a phenylalanine leads to a more hydrophobic environment of ring D in the iRFP mutant. Here, the structural model for iRFP shows a highly perturbed hydrogen bond network around the carbonyl group at ring D (Supporting Information, Figure S16). According to the statistics, the number of water molecules close (within a 5 Å distance, see Table 2) to the carbonyl group is reduced by one

Table 2. Statistics of Single and Double Hydrogen Bond Interactions between Carbonyl Groups of BV and the Environment in the PG-P2 and iRFP Models during the Production Run of the MD Simulations (60 ns–100 ns)^a

		C=O (A)		C=O (D)	
		WT	iRFP	WT	iRFP
number of H-bond events	no interaction	158	195	166	392
	single	212	181	230	8
	double	30	14	4	0
occupancy		58%	49%	59%	2%
minimum H-bond donor—acceptor distance (Å)		2.75	2.77	2.76	2.69

^aHydrogen bonds are defined by considering a donor—acceptor distance <3.0 Å and an angle cutoff of 20°.

in the mutant. Moreover, the C=O(D) does not form any hydrogen bond neither with the protein nor with water in the iRFP structure (Table 1). The lack of any hydrogen bond interactions of the ring D carbonyl function thus well explains the upshift of the C=O stretching mode in iRFP compared to PG-P2.

Additional structural changes refer to ring A and the A—B methine bridge. The spectra of the WT proteins PG-P2 and PGP-P2 and Agp1 display two bands attributable to the ring A C=O stretching modes, corresponding to two substates of slightly different structures or environmental interactions of the carbonyl group. It is therefore tempting to relate these two substates with a structural heterogeneity at the A—B methine bridge that may be derived from the 1640/1650 cm^{-1} band pair (vide supra). As judged from the spectra both in the C=O and the A—B stretching region, such a structural heterogeneity is much less pronounced for iRFP than for PG-P2 (PGP-P2). This conclusion is again consistent with findings from the MD simulations, which indicate a more rigid fixation of the chromophore within the protein. This is reflected by the much lower rmsf values for the carbon atom positions of the chromophore in the mutant compared to the wild-type protein. Specifically, for ring A and ring D, these values are lowered by ca. 30% in the mutant.

For the fluorescence-optimized iRFP and the “non-fluorescent” PG-P2, the temperature-dependent variations in the RR spectra are largely restricted to minor frequency shifts and the expected effects on the band widths. Furthermore, the fluorescence intensity increases by the same factor for both proteins upon temperature lowering from +10 to −140 °C. These findings can be understood in terms of a reduced mobility of the chromophore in the binding pocket at low temperature. However, there are no indications for temperature-dependent changes of the structural heterogeneity implying that the distribution among the various substates is largely the same at ambient temperature and −140 °C. Nevertheless, the RR and fluorescence spectroscopic data are consistent with the view that the substates constituting the chromophore heterogeneity differ with respect to the photo-physical properties, specifically fluorescence and photochemical quantum yields.

Structural Parameters Controlling the Fluorescence Properties. To increase the fluorescence quantum yield, the competing processes (that is, photoisomerisation and internal conversion of the excited state) must be slowed down. The main factors that influence the interplay of the various excited state processes have been recently discussed by Auldridge et al.⁹

Photoisomerisation is readily impaired by substituting the highly conserved Asp202 by any other amino acid. This is primarily attributed to the lack of a carboxyl side chain at a proper position for stabilizing the (distorted) ZZE_{ss} configuration in the excited state via interaction with the ring D N—H group. The second effect of a substitution at this position is the reorganization of the local hydrogen bond network, which may perturb an important thermal deactivation channel via excited state proton transfer of the cofactor to a nearby water molecule or the carbonyl function of the amino acid at position 202.¹¹ A distortion of the hydrogen bond interactions, specifically of the ring A carbonyl, has been demonstrated by the crystallographic analysis of the fluorescing CBD variant D207H of DrBphP. Although comparable changes in the hydrogen bond interactions cannot be derived from the present theoretical analysis, a perturbation of the decay channel via excited state proton transfer cannot be ruled out for iRFP^{12,14} because the RR spectra do in fact indicate structural changes of the A—B methine bridge and the ring A carbonyl. However, as a main conclusion of this work, we suggest that the increased rigidity of the chromophore in particular at the terminal rings A and D disfavors internal conversion as an energy dissipation pathway. A more rigid embedment of the chromophore into the protein matrix would also stabilize the ZZE_{ss} configuration and thus the Pr state, which is assumed to be the third factor relevant for increasing the fluorescence quantum yield. Here, the substitution of the tyrosine residue at position 258 by a phenylalanine, which also hinders photoisomerisation,¹⁴ may play an important role by strengthening the hydrophobic interactions with ring D and providing a tighter packing of this part of the chromophore.

The previous crystallographic study on fluorescent CBD variants of DrBphP has demonstrated that the effects of single amino acid substitutions on the structure of the chromophore pocket and the photophysical properties are not just additive such that the consequences of multiple substitutions can hardly be predicted.⁹ As an alternative to the time-consuming determination of the crystal structure, RR spectroscopy represents a rapid approach for correlating specific structural parameters with the fluorescent properties of the chromophore even though more systematic studies are required. Such studies may not necessarily be restricted to establish relationships between specific RR marker bands and the fluorescence yield. Moreover, the structural basis of other photophysical properties that are important for potential applications of phytochromes as fluorescence labels, such as the energy of the absorption and fluorescence maxima, is as well reflected by the RR spectra as recently shown for a cyanobacteriochrome.⁴¹ In this way, RR spectroscopy may become an important tool for the rational design and evolution of phytochrome-based fluorescence markers.

■ ASSOCIATED CONTENT

■ Supporting Information

Figures containing additional RR spectra, fluorescence data, plots resulting from the statistical analysis of the BV structure along the MD simulations, and description of the effects of the point mutations on the chromophore binding pocket. This material is available free of charge via the Internet at <http://pubs.acs.org>.

■ AUTHOR INFORMATION

Corresponding Author

*P. Hildebrandt. Phone: +49-30-314-21419. Fax: +49-30-314-21122. E-mail: Hildebrandt@chem.tu-berlin.de.

Author Contributions

[§]Equal contribution to this work.

Funding

The work was supported by the deutsche Forschungsgemeinschaft via the SFB1078 (M.A.M.; P.H.) and the Cluster of Excellence “Unifying Concepts in Catalysis” (T.F.)

Notes

The authors declare no competing financial interest.

■ ACKNOWLEDGMENTS

The authors thank the “Norddeutscher Verbund für Hoch- und Höchstleistungsrechnen” (HLRN) for providing computer power and Neslihan N. Tavraz for technical support.

■ ABBREVIATIONS

Agp1, bacteriophytochrome P1 from *Agrobacterium tumefaciens*; BV, biliverdin; CBD, chromophore binding domain; DrBphP, bacteriophytochrome from *Deinococcus radiodurans*; EDTA, ethylenediaminetetraacetic acid; GAF, cGMP-specific phosphodiesterases, adenylate cyclases, formate hydrogen lyase transcription activator; GFP, green-fluorescent protein; HOOP, hydrogen-out-of-plane vibrational mode; iRFP, fluorescence-optimized mutant of bacteriophytochrome P2 from *Rhodospseudomonas palustris*; MD, molecular dynamics (simulation); Nd:YAG, neodymium-doped yttrium aluminum garnet; N—H ip, nitrogen—hydrogen in plane bending; NPT, isothermic-isobaric ensemble; OD, optical density; PAS, PER/ARNT/SIM protein domain; PG-P2 (PGP-P2), PAS-GAF (PAS-GAF-PHY) fragment of bacteriophytochrome P2 from *Rhodospseudomonas palustris*; PHY, phytochrome-specific domain; Pr (Pfr), red-absorbing (far-red-absorbing) states of phytochromes; rmsd, root mean square deviations; rmsf, root mean square fluctuations; RbBphP2 (RbBphP3, RbBphP6), bacteriophytochrome P2 (P3, P6) from *Rhodospseudomonas palustris*; RR, resonance Raman; SAR, specific absorption ratio.

■ REFERENCES

- (1) Giepmans, B. N.; Adams, S. R.; Ellisman, M. H.; and Tsien, R. Y. (2006) The fluorescent toolbox for assessing protein location and function. *Science* 312, 317–324.
- (2) Stepanenko, O. V., Schcherbakova, D. M., Kuznetsova, I. M., and Verkhusha, V. V. (2011) Modern fluorescent proteins: from chromophore formation to novel intracellular applications. *Biotechniques* 51, 313–318.
- (3) Shcherbakova, D. M., Subach, O. M., and Verkhusha, V. V. (2012) Red fluorescent proteins: advanced imaging applications and future design. *Angew. Chem., Int. Ed.* 51, 10724–10738.
- (4) Filonov, G. S., Piatkevich, K. D., Ting, L. M., Zhang, J., Kim, K., and Verkhusha, V. V. (2011) Bright and stable near-infrared fluorescent protein for in vivo imaging. *Nat. Biotechnol.* 29, 757–761.
- (5) Shu, X., Royant, A., Lin, M. Z., Aguilera, T. A., Lev-Ram, V., Steinbach, P. A., and Tsien, R. Y. (2009) Mammalian Expression of Infrared Fluorescent Proteins Engineered from a Bacterial Phytochrome. *Science* 324, 804–807.
- (6) Shcherbakova, D. M., and Verkhusha, V. V. (2013) Near-infrared fluorescent proteins for multicolor in vivo imaging. *Nat. Methods* 10, 751–754.
- (7) Losi, A., Gärtner, W., Raffelberg, S., Zanacchi, F. C., Bianchini, P., Diaspro, A., Mandalari, C., Abbruzzetti, S., and Viappiani, C. (2013) A

photochromic bacterial photoreceptor with potential for super-resolution microscopy. *Photochem. Photobiol. Sci.* 12, 231–235.

(8) Rockwell, N., and Lagarias, J. (2010) A Brief History of Phytochromes. *ChemPhysChem* 11, 1172–1180.

(9) Auldridge, M. E., Satyshur, K. A., Anstrom, D. M., and Forest, K. T. (2012) Structure-guided engineering enhances phytochrome-based infrared fluorescent protein. *J. Biol. Chem.* 287, 7000–7009.

(10) Filonov, G. S., Krumholz, A., Xia, J., Yao, J., Wang, L. V., and Verkhusha, V. V. (2012) Deep-tissue photoacoustic tomography of a genetically encoded near-infrared fluorescent probe. *Angew. Chem., Int. Ed.* 51, 1448–1451.

(11) Toh, K. C., Stojkovic, E. A., van Stokkuma, I. H. M., Moffat, K., and Kennis, J. T. M. (2010) Proton-transfer and hydrogen-bond interactions determine fluorescence quantum yield and photochemical efficiency of bacteriophytochrome. *Proc. Natl. Acad. Sci. U. S. A.* 107, 9170–9175.

(12) Toh, K. C., Stojkovic, E. A., Rupenyan, A. B., van Stokkum, I. H. M., Salumbides, M., Groot, M. L., Moffat, K., and Kennis, J. T. M. (2011) Primary Reactions of Bacteriophytochrome Observed with Ultrafast Mid-Infrared Spectroscopy. *J. Phys. Chem. A* 115, 3778–3786.

(13) Lehtivuori, H., Rissanen, I., Takala, H., Bamford, J., Tkachenko, N. V., and Ihalainen, J. A. (2013) Fluorescence Properties of the Chromophore-Binding Domain of Bacteriophytochrome from *Deinococcus radiodurans*. *J. Phys. Chem. B* 117, 11049–11057.

(14) Toh, K. C., Stojkovic, E. A., van Stokkum, I. H. M., Moffat, K., and Kennis, J. T. M. (2011) *Phys. Chem. Chem. Phys.* 13, 11985–11997.

(15) Giraud, E., Zappa, S., Vuillet, L., Adriano, J. M., Hannibal, L., Fardoux, J., Berthomieu, C., Bouyer, P., Pignol, D., and Vermeglio, A. (2005) A new type of bacteriophytochrome acts in tandem with a classical bacteriophytochrome to control the antennae synthesis in *Rhodospseudomonas palustris*. *J. Biol. Chem.* 280, 32389–32397.

(16) Raab, D., Graf, M., Notka, F., Schödl, T., and Wagner, R. (2010) The GeneOptimizer algorithm: using a sliding window approach to cope with the vast sequence space in multiparameter DNA sequence optimization. *Syst. Synth. Biol.* 4, 215–225.

(17) Noack, S., Michael, N., Rosen, R., and Lamparter, T. (2007) Protein conformational changes of *Agrobacterium* phytochrome Agp1 during chromophore assembly and photoconversion. *Biochemistry* 46, 4164–4176.

(18) Phillips, J. C., Braun, R., Wang, W., Gumbart, J., Tajkhorshid, E., Villa, E., Chipot, C., Skeel, R. D., Kale, L., and Schulten, K. (2005) Scalable molecular dynamics with NAMD. *J. Comput. Chem.* 26, 1781–1802.

(19) NIH Center for Macromolecular Modeling & Bioinformatics, University of Illinois at Urbana–Champaign. <http://www.ks.uiuc.edu/Research/namd/> (2013).

(20) MacKerell, A. D., Jr., Bashford, D., Bellott, M., Dunbrack, R. L., Jr., Evanseck, J. D., Field, M. J., Fischer, S., Gao, J., Guo, H., Ha, S., Joseph-McCarthy, D., Kuchnir, L., Kucsera, K., Lau, F. T. K., Mattos, C., Michnick, S., Ngo, T., Nguyen, D. T., Prodhom, B., Reiher, W. E. I, Roux, B., Schlenkrich, M., Smith, J. C., Stote, R., Straub, J., Watanabe, H., and Karplus, M. (1998) All-Atom Empirical Potential for Molecular Modeling and Dynamics Studies of Proteins. *J. Phys. Chem. B* 102, 3586–3616.

(21) Kaminski, S., Daminelli-Widany, G., and Mroginiski, M. A. (2009) Molecular Dynamics Simulations of the Chromophore Binding Site of *Deinococcus radiodurans* Bacteriophytochrome Using New Force Field Parameters for the Phytychromobilin Chromophore. *J. Phys. Chem. B* 113, 945–958.

(22) Bellini, D., and Papiz, M. Z. (2012) Dimerization properties of the RbBphP2 chromophore-binding domain crystallized by homologue-directed mutagenesis. *Acta Crystallogr., Sect. D: Biol. Crystallogr.* 68, 1058–1066.

(23) Humphrey, W., Dalke, A., and Schulten, K. (1996) VMD: Visual molecular dynamics. *J. Mol. Graph.* 14, 33–38.

(24) Jorgensen, W. L., Chandrasekhar, J., Madura, J. D., Impey, R. W., and Klein, M. L. (1983) Comparison of Simple Potential Functions for Simulating Liquid Water. *J. Chem. Phys.* 79, 926–935.

(25) Darden, T. Y. D., and Pedersen, L. (1993) Particle Mesh Ewald - An N·Log(N) Method for Ewald Sums in Large Systems. *J. Chem. Phys.* 98, 10089–10092.

(26) Van Gunsteren, W. F., and Berendsen, H. J. C. (1977) Algorithms for macromolecular dynamics and constraint dynamics. *Mol. Phys.* 34, 1311–1327.

(27) Feller, S. E., Zhang, Y. H., Pastor, R. W., and Brooks, B. R. (1995) Constant-Pressure Molecular-Dynamics Simulation - the Langevin Piston Method. *J. Chem. Phys.* 103, 4613–4621.

(28) Wagner, J. R., Zhang, J. R., von Stetten, D., Guenther, M., Murgida, D. H., Mroginiski, M. A., Walker, J. M., Forest, K. T., Hildebrandt, P., and Vierstra, R. D. (2008) Mutational analysis of *Deinococcus radiodurans* bacteriophytochrome reveals key amino acids necessary for the photochromicity and proton exchange cycle of phytochromes. *J. Biol. Chem.* 283, 12212–12226.

(29) Wagner, J. R., Zhang, J. R., Brunzelle, J. S., Vierstra, R. D., and Forest, K. T. (2007) High resolution structure of *Deinococcus bacteriophytochrome* yields new insights into phytochrome architecture and evolution. *J. Biol. Chem.* 282, 12298–12309.

(30) Yang, X., Stojkovic, E. A., Kuk, J., and Moffat, K. (2007) Crystal structure of the chromophore binding domain of an unusual bacteriophytochrome, RbBphP3, reveals residues that modulate photoconversion. *Proc. Natl. Acad. Sci. U. S. A.* 104, 12571–12576.

(31) Essen, L. O., Hughes, J., and Mailliet, J. (2008) The structure of a complete phytochrome sensory module in the Pr ground state. *Proc. Natl. Acad. Sci. U. S. A.* 105, 14709–14714.

(32) Mroginiski, M. A., von Stetten, D., Escobar, F. V., Strauss, H. M., Kaminski, S., Scheerer, P., Günther, M., Murgida, D. H., Schmieder, P., Bongards, C., Gärtner, W., Mailliet, J., Hughes, J., Essen, L. O., and Hildebrandt, P. (2009) Chromophore Structure of Cyanobacterial Phytochrome Cph1 in the Pr State: Reconciling Structural and Spectroscopic Data by QM/MM Calculations. *Biophys. J.* 96, 4153–4163.

(33) Mroginiski, M. A., Kaminski, S., von Stetten, D., Ringsdorf, S., Gärtner, W., Essen, L. O., and Hildebrandt, P. (2011) Structure of the Chromophore Binding Pocket in the Pr State of Plant Phytochrome phyA. *J. Phys. Chem. B* 115, 1220–1231.

(34) Mroginiski, M. A., von Stetten, D., Kaminski, S., Velazquez Escobar, F., Michael, N., Daminelli-Widany, G., and Hildebrandt, P. (2011) Elucidating photoinduced structural changes in phytochromes by the combined application of resonance Raman spectroscopy and theoretical methods. *J. Mol. Struct.* 993, 15–25.

(35) Salewski, J., Velazquez, F., Kaminski, S., von Stetten, D., Keidel, A., Rippers, Y., Michael, N., Scheerer, P., Piwowarski, P., Bartl, F., Frankenberg-Dinkel, N., Ringsdorf, S., Gärtner, W., Lamparter, T., Mroginiski, M. A., and Hildebrandt, P. (2013) The structure of the biliverdin cofactor in the Pfr state of bathy and prototypical phytochromes. *J. Biol. Chem.* 288, 16800–16814.

(36) Schwinte, P., Foerstendorf, H., Hussain, Z., Gärtner, W., Mroginiski, M. A., Hildebrandt, P., and Siebert, F. (2008) FTIR study of the photoinduced processes of plant phytochrome phyA using isotope-labeled bilins and density functional theory calculations. *Biophys. J.* 95, 1256–1267.

(37) von Stetten, D., Guenther, M., Scheerer, P., Murgida, D. H., Mroginiski, M. A., Krauss, N., Lamparter, T., Zhang, J., Anstrom, D. M., Vierstra, R. D., Forest, K. T., and Hildebrandt, P. (2008) Chromophore heterogeneity and photoconversion in phytochrome crystals and solution studied by resonance Raman spectroscopy. *Angew. Chem., Int. Ed.* 47, 4753–4755.

(38) Piwowarski, P., Ritter, E., Hofmann, K. P., Hildebrandt, P., von Stetten, P., Scheerer, P., Michael, N., Lamparter, T., and Bartl, F. (2010) Light Induced Activation of Bacterial Phytochrome Agp1 Monitored by Static and Time Resolved FTIR Spectroscopy. *ChemPhysChem* 11, 1207–1214.

(39) Siamwiza, M. N., Lord, R. C., Chen, M. C., Takamatsu, T., Harada, I., Matsuura, H., and Shimanouchi, T. (1975) Interpretation of the doublet at 850 and 830 cm⁻¹ in the Raman spectra of tyrosyl residues in proteins and certain model compounds. *Biochemistry* 14, 4870–4876.

(40) Hildebrandt, P., and Stockburger, M. (1984) Role of Water in Bacteriorhodopsin Chromophore: A Resonance Raman Study. *Biochemistry* 23, 5539–5548.

(41) Velazquez Escobar, F., Utesch, T., Narikawa, R., Ikeuchi, M., Mroginiski, M. A., Gärtner, W., and Hildebrandt, P. (2013) Photoconversion mechanism of the second GAF domain of cyanobacteriochrome AnPixJ and the cofactor structure of its green-absorbing state. *Biochemistry* 52, 4871–4880.